Modeling the Aeroelastic Response of a Cantilevered Plate Using the Vortex Lattice Method and Modal Analysis

by

Shixi Jin

Department of Mechanical Engineering and Materials Science
Duke University

Defense Date: April 1st, 2024

Approved:

Earl H. Dowell, Advisor

Kenneth C. Hall

George Delagrammatikas

Thesis submitted in partial fulfillment of the requirements for the degree of Master of Science in the Department of Mechanical Engineering and Material Science in The Graduate School of Duke University
2024

ABSTRACT

Modeling the Aeroelastic Response of a Cantilevered Plate Using the Vortex Lattice Method and Modal Analysis

by

Shixi Jin

Department of Mechanical Engineering and Materials Science
Duke University

Defense Date: April 1st, 2024

Approved:

Earl H. Dowell, Advisor

Kenneth C. Hall

George Delagrammatikas

An abstract of a thesis submitted in partial fulfillment of the requirements for the degree of Master of Science in the Department of Mechanical Engineering and Material Science in The Graduate School of
Duke University
2024

Abstract

The creation of an aeroelastic model for a cantilevered plate under a uniform flow is discussed. Starting with solving the aerodynamic load distribution over the plate using the vortex lattice method, this paper continues with discussing a structural model for the nonlinear behavior of an inextensible plate which utilizes the Euler-Lagrange equation and the Rayleigh-Ritz method to derive the equations of motion. The computation model discussed in this thesis couples the vortex lattice method with structural analysis to simulate the aeroelastic response of a thin plate.

Computational results are shown which capture the time history of plate deflection at different flow velocities. The development of flutter dynamic's instability is also observed by mapping limit cycle oscillation amplitudes at varying flow velocities and compared with experimental values from past studies.

Contents

List of Tables

List of Figures

Nomenclature

AR	Aspect ratio of the plate
AOA	Angle of attack
b	Span length of the plate
c	Chord length of the plate
dx	Length of one vortex element in the chordwise direction
dy	Length of one vortex element in the spanwise direction
E	Young's modulus
f	Constraint force
h	Plate thickness
I	Plate inertia
m	Mass per unit length
n_x	The number of vortex element along the chord
n_y	The number of vortex elements along the span
N	The total number of vortex elements on the plate and in the wake, combined
N_{plate}	The total number of vortex elements on the plate
p	Pressure along the plate
q	Transverse deflection modal amplitude
t	Time
T	Kinetic energy
u, w, λ	The coordinates used for structural analysis; the longitudinal direction, the transverse direction, and the Lagrange multiplier
U	Streamwise flow speed
V	Potential energy
W	Downwash

x, y	The chordwise and spanwise coordinates, respectively
α	Relaxation factor
ζ	Damping coefficient
Γ	Vortex strength
ω	Natural frequency
ρ, ρ_s	Air density, plate density
ν	Poisson's ratio
Ψ_i^u	Shape functions in the u, w, and λ directions

Acknowledgements

I'd like to express my deep gratitude to my advisor and mentor, Dr. Earl Dowell, for his persistent support and kind encouragement that made this learning journey a cherished experience, and Dr. Kenneth Hall for his invaluable guidance on the concepts used in this thesis. I'd also like to thank Luisa Piccolo Serafim, my PhD student colleague and mentor, for her direction and assistance are instrumental in navigating through this research.

1. Introduction

The study of aeroelastic phenomena has played a significant role in aeronautical applications, civil, mechanical, and many other fields of engineering that pique interest in fluid-structure interactions. Although traditionally, aeroelasticity is more associated with undesirable phenomena such as flutter and divergence, more attention has been gathered on its beneficial effects in recent years. For example, the discussion of an aeroelastic model in this thesis was originally motivated by a study about energy harvesting which involves the extraction of energy from structures in limit cycle oscillations (LCO) using piezoelectric components, explored by Tang and Dowell [1] and Dunnmon et al [2].

To address the need for both predicting failure and utilizing aeroelastic effects, it is most beneficial to create a computational model which will predict the response of a structure undergoing such effects. This thesis discusses the development of an aeroelastic model for a simplified system: a thin, inextensible, rectangular plate fixed at the leading edge under the effect of a uniform and constant flow in the chordwise direction (See Figure 1).

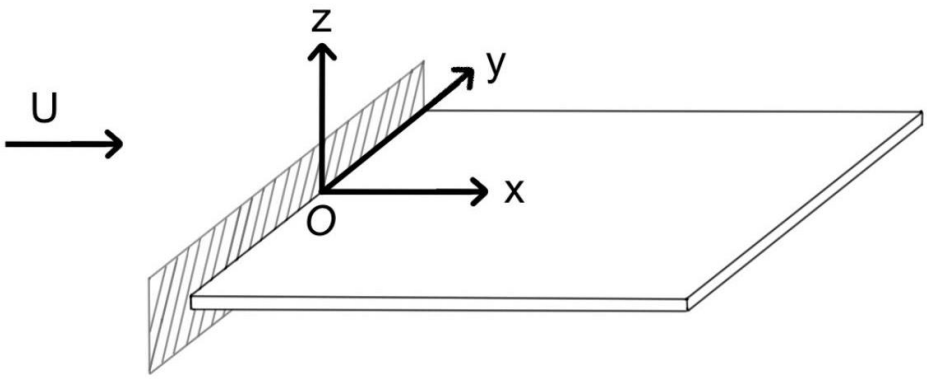

Figure 1: plate configuration for the aeroelastic analysis

The aeroelastic model computes the plate's physical response to the combination of aerodynamic load and structural forces by coupling the vortex lattice method (VLM), which is used to find the aerodynamic loads on the plate, with a structural model derived from the Euler-Lagrange equation and the Rayleigh-Ritz method. At each time step, the aerodynamic load along the plate, calculated using VLM, instigates the plate to deflect, and the deflection will change the aerodynamic loads for the next time step, and so on.

For the remainer of this thesis, Chapter 2 discusses the implementation of VLM to solve for the aerodynamic effects on the plate, whereas Chapter 3 describes the structural analysis solving for the physical response of the plate. Then, the coupling of the two models, aerodynamic and structural, is discussed for the computation of aeroelastic responses. Computational results are then presented and compared with experimental results from past works. The limitations and uncertainties for this model are also discussed along with conclusions drawn from the results of this study.

2. The Vortex Lattice Method

The vortex lattice method (VLM) describes incompressible, inviscid, and irrotational flows with a system of horseshoe vortices starting at the quarter chord of a panel and trailing behind it. A reaction vortex is set at the three-quarter chord and the half span of the panel to balance the downwash created by the system of vortices (See Figure 2). This technique allows the vortex strength on each panel to be computed with relative ease and accuracy. Then, knowing the vortex strength along the wing, one can compute the aerodynamic loading distribution on the wing. See Hall [3] for an in depth study of VLM.

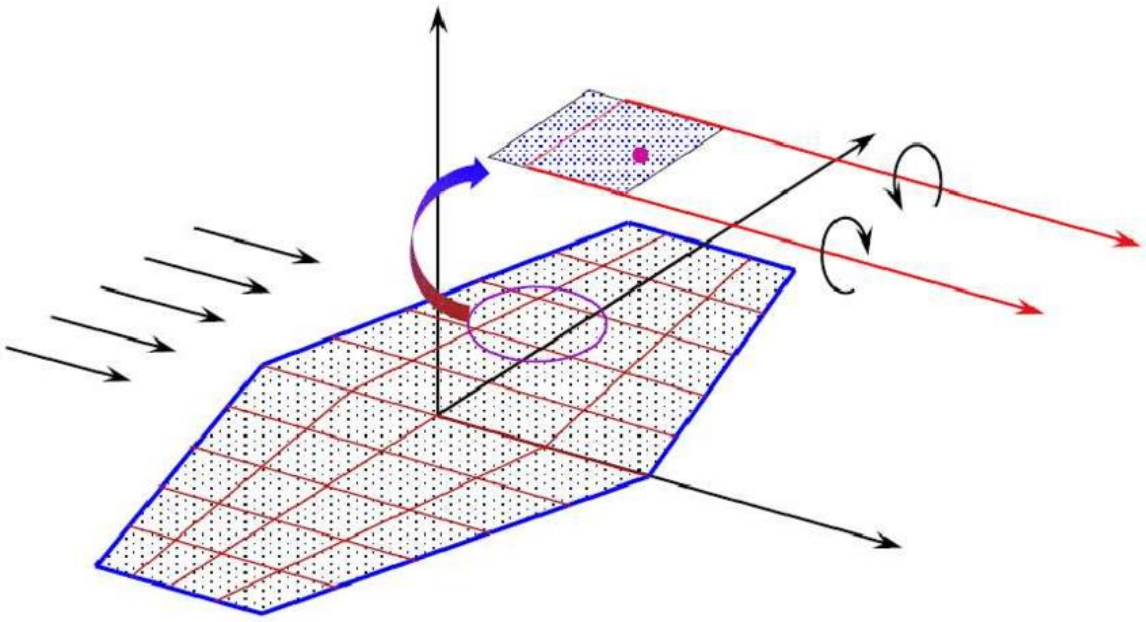

Figure 2: Schematic of the Vortex Lattice Method [4]

2.1 Solving for Vortex Strength

For the cantilevered plate model, the plate and the wake region behind it are meshed into rectangular elements of equal dimensions, dx and dy, and on each element, two point vortices are placed at the quarter chord. The flow about this system of elements is considered in four sections:

1) the vortices on the plate, 2) the first column of vortices in the wake, 3) the vortices in the main wake region, and 4) the last column of vortices in the wake (See Figure 3).

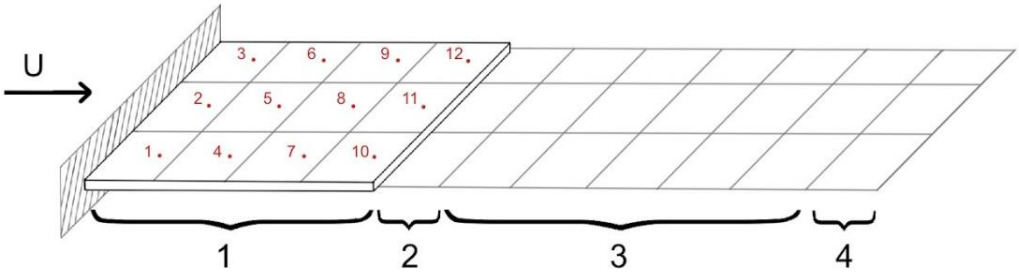

Figure 3: Meshing and sectioning of the plate and the wake

On every element in the first section (along the plate), a collocation point is set at the three-quarter chord and the mid span, where a reaction vortex is formed, whose induced velocities balances the downwash created by the plate motion. The relationship between the vortex strength on each panel and the downwash can be described with the following equation:

$$W_i^{t+1} = \sum_{j=1}^{N} K_{ij} \Gamma_j^{t+1} \qquad \text{for i = 1, …, } N_{plate} \tag{2.1}$$

Where N_{plate} and N are the total number of vortex elements on the plate only and in the entire system, respectively, W_i^{t+1} is the downwash at the i-th collocation point at the t+1-th time step, $\Gamma_j^{t+1}$is the vortex strength acting on the j-th collocation point at the t+1-th time step, and K_{ij} is a kernel function, which in this scenario, is a matrix built from the following relationship:

$$K_{ij} = \frac{-1}{4\pi(y_i - y_{ja})}\left[1 + \frac{\sqrt{(x_i - x_{ja})^2 + (y_i - y_{ja})^2}}{x_i - x_{ja}}\right] + \frac{1}{4\pi(y_i - y_{jb})}\left[1 + \frac{\sqrt{(x_i - x_{ja})^2 + (y_i - y_{jb})^2}}{x_i - x_{ja}}\right] \tag{2.2}$$

Where x_i, y_i, x_{ja}, y_{ja}, and y_{jb} are locations for the i-th collocation point and the j-th trailing vortex.

Along the first column of vortex elements in the wake, the vortex strengths can be modeled by the following equation:

$$\Gamma_i^{t+1} = -\sum_{j=1}^{n_x}(\Gamma_{i-j*n_y}^{t+1} - \Gamma_{i-j*n_y}^{t}) \qquad \text{for i} = N_{plate} + 1, \ldots, N_{plate} + n_y \qquad (2.3)$$

Where n_x is the number of vortex elements along the chord of the plate, and n_y is the number of vortex elements along the span. The vortex strength equates to the negative accumulation of the difference between the vortex strength at each collocation point in the columns before the i-th collocation point and the vortex strength at the same point from the previous time step. For example, if the system is meshed with 2x3 elements along the plate, the vortex strength at collocation point 7 at the t+1-th time step would be $-\left[(\Gamma_1^{t+1} - \Gamma_1^{t+1}) + (\Gamma_3^{t+1} - \Gamma_3^{t+1}) + \left(\Gamma_5^{t+1} - \Gamma_5^{t+1}\right)\right]$.

Then, starting from the second column of vortex elements to the second to last column in the wake region, the vortex strength at each element can be described by the following equation:

$$\Gamma_i^{t+1} = \Gamma_{i-n_y}^{t} \qquad \text{for i} = N_{plate} + n_y + 1, \ldots, \text{N} - n_y - 1 \qquad (2.4)$$

Where the vortex strength at the i-th collocation point at the t+1-th time step, Γ_i^{t+1}, equates the vortex strength at the collocation point in the previous column, at the previous time step.

Finally, at the last column in the wake, the vortex strength can be described by the following equation:

$$\Gamma_i^{t+1} = \Gamma_{i-1}^{t} + \alpha\Gamma_i^{t} \qquad \text{for i} = \text{N} - \text{n}, \ldots, \text{N} \qquad (2.5)$$

Where the term α is a relaxation factor, a constant typically within the range of $0.95 < \alpha < 1.0$.

By rearranging equations 2.1 and 2.3 – 2.5, the relationship between vortex strength and downwash can be put into the following form:

$$A\Gamma^{n+1} + B\Gamma^{n} = W^{n+1} \qquad (2.6)$$

Where A and B are aerodynamic coefficient matrices. For instance, for a system with 2x3 elements on the plate and 2x4 elements in the wake, the coefficient matrices look like the following:

A =

$$[K_{ij}]_{6x14}$$

1	0	1	0	1	0	1	0	0	0	0	0	0	0
0	1	0	1	0	1	0	1	0	0	0	0	0	0
0	0	0	0	0	0	0	0	1	0	0	0	0	0
0	0	0	0	0	0	0	0	0	1	0	0	0	0
0	0	0	0	0	0	0	0	0	0	1	0	0	0
0	0	0	0	0	0	0	0	0	0	0	1	0	0
0	0	0	0	0	0	0	0	0	0	0	0	1	0
0	0	0	0	0	0	0	0	0	0	0	0	0	1

And

B =

$$[0]_{6x14}$$

-1	0	-1	0	-1	0	0	0	0	0	0	0	0	0
0	-1	0	-1	0	-1	0	0	0	0	0	0	0	0
0	0	0	0	0	0	-1	0	0	0	0	0	0	0
0	0	0	0	0	0	0	-1	0	0	0	0	0	0
0	0	0	0	0	0	0	0	-1	0	0	0	0	0
0	0	0	0	0	0	0	0	0	-1	0	0	0	0
0	0	0	0	0	0	0	0	0	0	-1	0	-.992	0
0	0	0	0	0	0	0	0	0	0	0	-1	0	-.992

For $\alpha = 0.992$

Knowing A, B, and the downwash, which depends on the deflection of the plate, the vortex strength along the plate can be computed for each time step. More accurate values can be obtained for finer meshes.

2.2 Pressure Distribution

Knowing the vortex strength along the plate, the pressure distribution can be obtained using the following equation:

$$\frac{p}{\rho U^2} = \frac{dx}{U}\left[\left(\Gamma_i^{t+1} + \Gamma_i^{t}\right) + \sum_{j=1}^{i}\left(\Gamma_j^{t+1} - \Gamma_j^{t}\right)\right] \tag{2.7}$$

Applying this calculation at each step allows one to observe the pressure development along the plate.

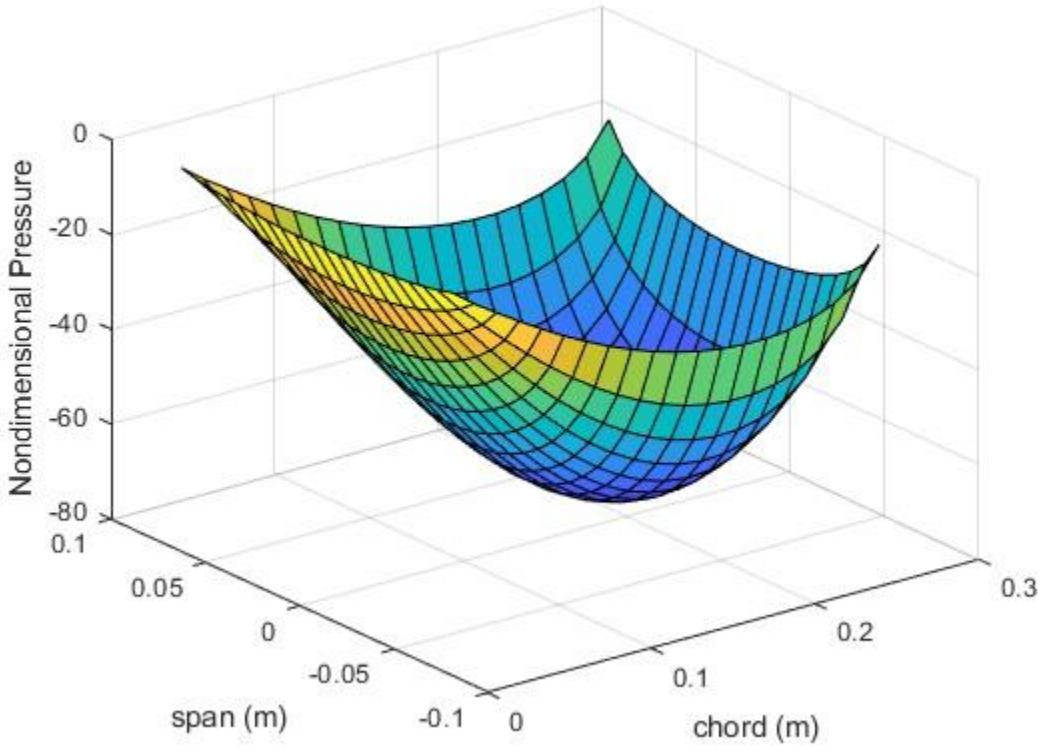

Figure 4: Converged pressure distribution over a cantilevered, rectangular plate

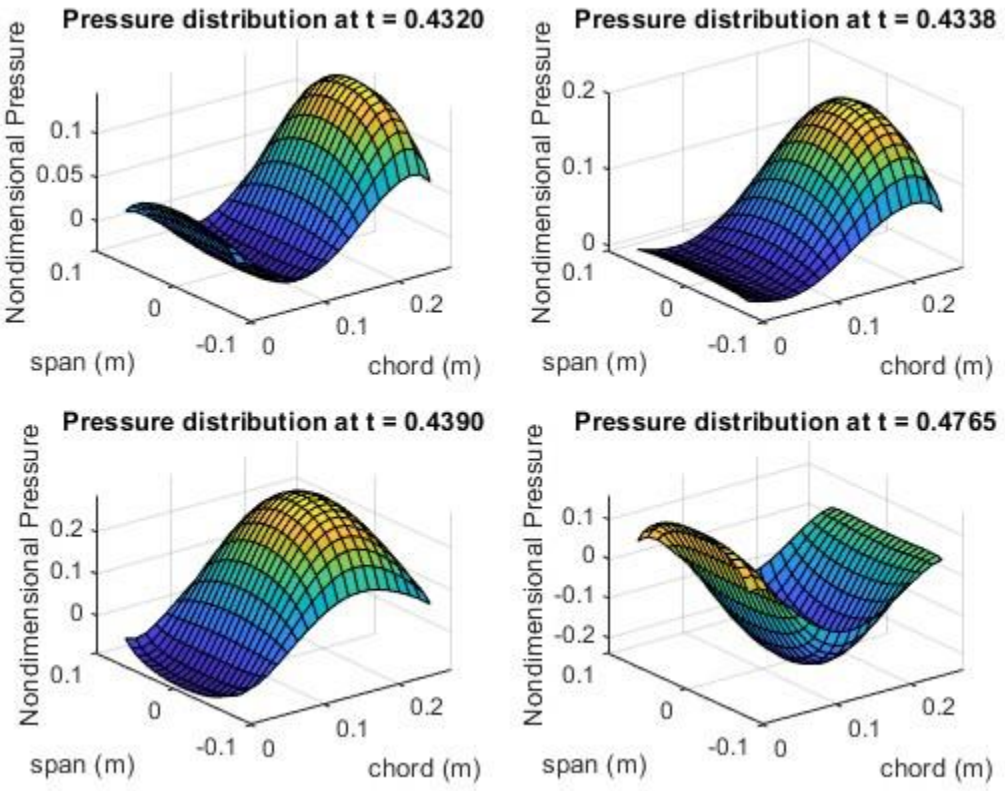

Figure 5: Pressure distribution for the coupled aeroelastic model at different times

Table 1: Plate and flow parameters

c	0.275 m
AR	0.5491
h	0.381e-3 m
E	70.6 GPa
ν	0.33
ρ	1.221 $\frac{kg}{m^3}$
ρ_s	2840 $\frac{kg}{m^3}$
U	25 $\frac{m}{s}$
α	0.992
ζ	0.005

n_x	20
n_y	20
N_{plate}	2000

Number of Modes in	
u	2
w	2
λ	2

Consider a steady flow case for the aerodynamic model: a cantilevered plate that is fixed in the first mode shape with a nondimensional tip deflection, $\frac{q}{c}$, of 0.25 (the deflection is given as

a step change at the first time step) and is free of structural effects. Inputting the computations from this chapter in a computing tool (MATLAB is used for this thesis) and marching for a sufficient number of time steps, the nondimensional pressure distribution along the plate reaches convergence and is shown in Figure 4. The parameters used for this case are listed in Table 1.

When structural properties of the plate are also considered, the pressure distribution is subject to change at each time step as the plate's deflection changes the downwash along the plate. For example, see Figure 5 for how pressure distribution varies at different times when coupled with structural forcing.

3. Structural Analysis

The computation method discussed in this chapter follows closely the work of Tang, McHugh and Dowell [5, 6, 7, 8], their nonlinear structural model of an inextensible cantilevered plate. The theory combines the Lagrange method with the Rayleigh-Ritz method in constructing the equations of motion, which are then used to solve for the physical response of the plate using MATLAB's ODE45 solver.

3.1 Defining the Euler-Lagrange Equations and the Modal Functions

The equations of motion for the cantilever plate are derived from the Euler-Lagrange equation:

$$\frac{d}{dt}\left(\frac{\partial \mathcal{L}}{\partial \dot{q}_i}\right) - \frac{\partial \mathcal{L}}{\partial q_i} = 0 \tag{3.1}$$

Where the q_i stands for the spatial coordinates, u and w, which are in the longitudinal and transverse directions, respectively, and λ, which is the Lagrange multiplier added for the inextensibility constraint of the plate. The Lagrangian $\mathcal{L}$ is given by:

$$\mathcal{L} = T - V + \int_0^c \lambda f dx \tag{3.2}$$

Where T, V, and λ are kinetic energy, potential energy, and the constraint force, respectively, and they can be expressed as the following:

$$T = \frac{1}{2}\int_0^c m(\dot{u}^2 + \dot{w}^2)dx \tag{3.3}$$

$$V = \frac{1}{2}\int_0^c EI(\frac{\partial^2 w}{\partial x^2})^2 \left[1 + \left(\frac{\partial w}{\partial x}\right)^2\right] dx \tag{3.4}$$

and

$$f = \frac{\partial u}{\partial x} + \frac{1}{2}(\frac{\partial w}{\partial x})^2 = 0 \tag{3.5}$$

is the constraint condition of zero longitudinal strain.

The coordinate terms u, w, and λ from equations 3.3 – 3.5 can be decomposed into modal forms and be written in the following equations:

$$u = \sum_i \Psi_i^u(x) u_i(t) \tag{3.6}$$

$$w = \sum_j \Psi_j^w(x) w_j(t) \tag{3.7}$$

$$\lambda = \sum_k \Psi_k^\lambda(x) \lambda_k(t) \tag{3.8}$$

Note that for all equations in Chapter 3 from equation 3.6 and beyond, the indices i, j, and k signify the number of modes in the u, w, and λ coordinates, respectively. For a cantilevered plate, the mode shapes can be described by the following functions:

$$\Psi_i^u = \sin\left(\frac{2i-1}{2}\pi\frac{x}{c}\right) \tag{3.9}$$

$$\Psi_j^w = \frac{1}{2}\left[\cosh\left(\beta_j\frac{x}{c}\right) - \cos\left(\beta_j\frac{x}{c}\right) + R_j\sin\left(\beta_j\frac{x}{c}\right) - R_j\sinh\left(\beta_j\frac{x}{c}\right)\right] \tag{3.10}$$

$$\Psi_k^\lambda = \sin\left[\frac{2k-1}{2}\pi\left(1-\frac{x}{c}\right)\right] \tag{3.11}$$

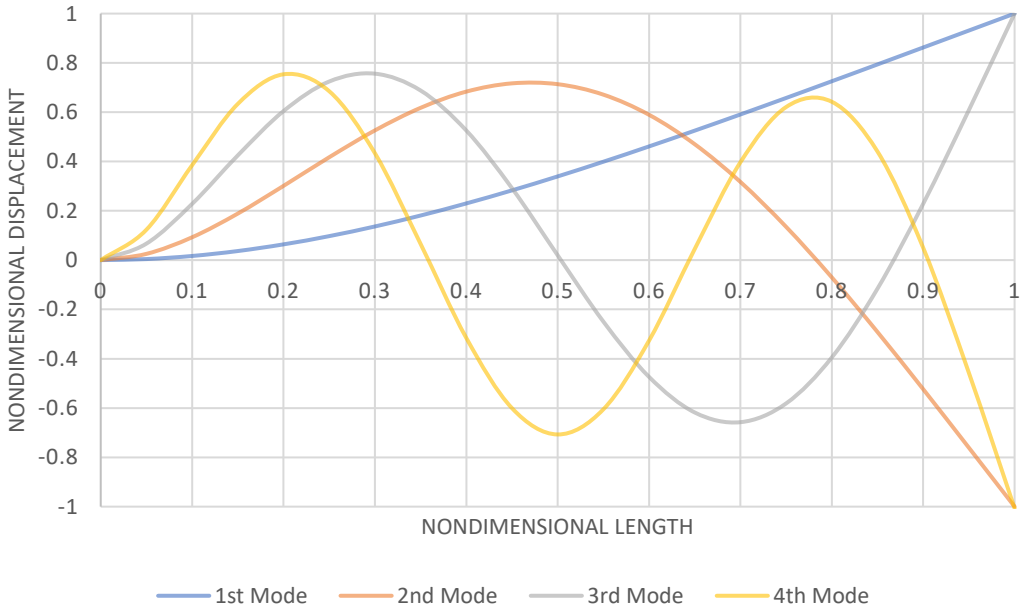

Figure 6: The first 4 natural mode shapes for the cantilevered plate

Where the β_j and R_j values can be solved from the following equations:

$$\cos(\beta_j)\cosh(\beta_j) + 1 = 0 \tag{3.12}$$

$$R_j = \frac{\cosh(\beta_j)+\cos(\beta_j)}{sinh(\beta_j)+sin(\beta_j)} \tag{3.13}$$

3.2 Deriving the Equations of Motion

As the coordinate terms and their shape functions are defined in equations 3.6 – 3.11, the energy equations (3.3 – 3.5) can be rewritten with the modal functions as shown below:

$$T = \frac{1}{2}\int_0^c m\left[\sum_{i1}\sum_{i2}\Psi_{i1}^{u}\Psi_{i2}^{u}\dot{u_{i1}}\dot{u_{i2}} + \sum_{j1}\sum_{j2}\Psi_{j1}^{w}\Psi_{j2}^{w}\dot{w_{j1}}\dot{w_{j2}}\right]dx \tag{3.14}$$

$$V = \frac{1}{2}\int_0^c EI\left(\sum_{j1}\sum_{j2}\Psi_{j1}^{w''}\Psi_{j2}^{w''}w_{j1}w_{j2} + \sum_{j1}\sum_{j2}\sum_{j3}\sum_{j4}\Psi_{j1}^{w''}\Psi_{j2}^{w''}\Psi_{j3}^{w'}\Psi_{j4}^{w'}w_{j1}w_{j2}w_{j3}w_{j4}\right)dx \tag{3.15}$$

$$f = \sum_i \Psi_{i1}^{u'}u_i + \frac{1}{2}\sum_{j1}\sum_{j2}\Psi_{j1}^{w'}\Psi_{j2}^{w'}w_{j1}w_{j2} \tag{3.16}$$

Then, to substitute the modal functions into equation 3.1, partial differentials of T, V, and the work done by f need to be taken. After simplifying the terms, the following partial derivatives are obtained:

$$\frac{d}{dt}\frac{\partial T}{\partial \dot{u_\iota}} = m\int_0^c \Psi_i^u\Psi_i^u dx\ddot{u_\iota} \tag{3.17}$$

$$\frac{d}{dt}\frac{\partial T}{\partial \dot{w_\jmath}} = m\int_0^c \Psi_j^w\Psi_j^w dx\ddot{w_j} \tag{3.18}$$

$$\frac{\partial V}{\partial w_j} = m\omega_j^2 w_j\int_0^c \Psi_j^w\Psi_j^w dx + \sum_{j1}\sum_{j2}\sum_{j3} EIw_{j1}w_{j2}w_{j3}\int_0^c(\Psi_{j1}^{w''}\Psi_{j2}^{w''}\Psi_{j3}^{w'}\Psi_j^{w'} + \Psi_{j1}^{w''}\Psi_{j2}^{w''}\Psi_{j3}^{w'}\Psi_j^{w'})dx \tag{3.19}$$

$$\frac{\partial}{\partial u_i}\left(\int_0^c \lambda f dx\right) = \sum_k \int_0^c \Psi_i^{u'}\Psi_k^{\lambda}dx\,\lambda_k \tag{3.20}$$

$$\frac{\partial}{\partial w_j}\left(\int_0^c \lambda f dx\right) = \sum_k\sum_{j1}\int_0^c \Psi_k^{\lambda}\Psi_{j1}^{w'}\Psi_j^{w'}\,dx\lambda_k w_{j1} \tag{3.21}$$

$$\frac{\partial}{\partial \lambda_k}\left(\int_0^c \lambda f dx\right) = \sum_i \int_0^c \Psi_k^{\lambda}\Psi_i^{u'}dx\,u_i + \frac{1}{2}\sum_{j1}\sum_{j2}\int_0^c \Psi_k^{\lambda}\Psi_{j1}^{w'}\Psi_{j2}^{w'}\,dxw_{j1}w_{j2} \tag{3.22}$$

For simplicity and efficiency of the computation, terms that only depend on the plate properties and boundary conditions are separated as coefficient matrices. These terms need only to be computed once and will not change at each time step of the aeroelastic simulation:

$$M_u = \int_0^c \Psi_i^u \Psi_i^u dx \tag{3.23}$$

$$M_w = \int_0^c \Psi_j^w \Psi_j^w dx \tag{3.24}$$

$$P = \int_0^c (\Psi_{j1}^{w''} \Psi_{j2}^{w''} \Psi_{j3}^{w'} \Psi_j^{w'} + \Psi_{j1}^{w''} \Psi_{j2}^{w''} \Psi_{j3}^{w'} \Psi_j^{w'}) dx \tag{3.25}$$

$$A_{ik} = \int_0^c \Psi_i^{u'} \Psi_k^{\lambda} dx \tag{3.26}$$

$$B_{kj1j} = \int_0^c \Psi_k^{\lambda} \Psi_{j1}^{w'} \Psi_j^{w'} dx \tag{3.27}$$

Thus, equations 3.17 – 3.22 become the following:

$$\frac{d}{dt}\frac{\partial T}{\partial \dot{u}_\iota} = mM_u \ddot{u}_\iota \tag{3.28}$$

$$\frac{d}{dt}\frac{\partial T}{\partial \dot{w}_j} = mM_w \ddot{w}_j \tag{3.29}$$

$$\frac{\partial V}{\partial w_j} = m\omega_j^2 M_w w_j + \sum_{j1}\sum_{j2}\sum_{j3} EIP w_{j1} w_{j2} w_{j3} \tag{3.30}$$

$$\frac{\partial}{\partial u_i}\left(\int_0^c \lambda f dx\right) = \sum_k A_{ik}\lambda_k \tag{3.31}$$

$$\frac{\partial}{\partial w_j}\left(\int_0^c \lambda f dx\right) = \sum_k \sum_{j1} B_{kj1j}\lambda_k w_{j1} \tag{3.32}$$

$$\frac{\partial}{\partial \lambda_k}\left(\int_0^c \lambda f dx\right) = \sum_i A_{ik} u_i + \frac{1}{2}\sum_{j1}\sum_{j2} B_{kj1j2} w_{j1} w_{j2} \tag{3.33}$$

Finally, by substituting equations 3.28 – 3.33 back into the Euler-Lagrange equation, the following system of equations can be obtained:

$$0 = mM_u \ddot{u}_\iota - \sum_k A_{ik}\lambda_k$$

$$0 = mM_w \ddot{w}_j + 2m\zeta_j \omega_j M_w \dot{w}_j + m\omega_j^2 M_w w_j + \sum_{j1}\sum_{j2}\sum_{j3} EIP w_{j1} w_{j2} w_{j3} - \sum_k \sum_{j1} B_{kj1j}\lambda_k w_{j1}$$

$$0 = \sum_i A_{ik} u_i + \frac{1}{2} \sum_{j1} \sum_{j2} B_{kj1j2} w_{j1} w_{j2}$$

(3.34)

From which, the equations of motion can be solved for. In the scope of this thesis, the transverse direction is the primary coordinate of interest, and it can be derived from equation 3.34 that

$$\{\ddot{w}\} = \left\{ M_w + \sum_{k1} B_{k1::} \sum_k \left[\left(\sum_{i1} \sum_{i2} A_{:i1} (M_u)^{-1} A_{i2} \right)^{-1} \sum_{j1} \sum_{j2} B_{:j1j2} w_{j1} w_{j2} \right] \right\}^{-1}$$
$$\left\{ -\omega^2 M_w w_j - 2\zeta\omega M_w \dot{w}_j - EI \sum_{j1} \sum_{j2} \sum_{j3} EIP w_{j1} w_{j2} w_{j3} \right.$$
$$\left. - \sum_j \sum_{k1} B_{k1j:} \sum_k \left[\left(\sum_{i1} \sum_{i2} A_{i1k} (M_u)^{-1} A_{i2k} \right)^{-1} \sum_{j1} \sum_{j2} B_{kj1j2} \dot{w_{j1}} \dot{w_{j2}} \right] w_j \right\}$$

(3.35)

Note that here, the damping coefficient $\zeta$and the natural frequencies ω are diagonal matrices where each entry corresponds to the value at the respective mode number. The first line, $\{M_w + \sum_{k1} B_{k1::} \sum_k [(\sum_{i1} \sum_{i2} A_{:i1} (M_u)^{-1} A_{i2})^{-1} \sum_{j1} \sum_{j2} B_{:j1j2} w_{j1} w_{j2}]\}$ is the mass matrix for the model.

When the aerodynamic forcings are also considered, equation 3.35 becomes the following:

$$\{\ddot{w}\} = [Mass]^{-1} \left\{ Q_j - \omega^2 M_w w_j - 2\zeta\omega M_w \dot{w}_j - EI \sum_{j1} \sum_{j2} \sum_{j3} EIP w_{j1} w_{j2} w_{j3} \right.$$
$$\left. - \sum_j \sum_{k1} B_{k1j:} \sum_k \left[\left(\sum_{i1} \sum_{i2} A_{i1k} (M_u)^{-1} A_{i2k} \right)^{-1} \sum_{j1} \sum_{j2} B_{kj1j2} \dot{w_{j1}} \dot{w_{j2}} \right] w_j \right\}$$

(3.36)

Where the term Q_j describes the aerodynamic load and is given by

$$Q_j = \int_{-\frac{b}{2}}^{\frac{b}{2}} \int_0^c p\Psi_j(x,y)dxdy \tag{3.37}$$

Where p is determined by solving equation 2.7.

4. Model Implementation

4.1 Preprocessing

The following is a list of user inputs which are defined at the start of the computation:

- Plate geometry,
- Plate material properties (Young's Modulus, Poisson ratio, density),
- Fluid density,
- Flow speed,
- Number of elements in the x and y direction,
- Number of modes in each coordinate (u, w, λ),
- And the initial condition of the plate.

From the user input, meshes are produced along the plate, and from there, the aerodynamic coefficient matrices can be computed as they only rely on the plate's geometry and meshes. The structural coefficient matrices can also be solved as they only rely on the plate geometry and the number of modes.

4.2 Coupling Aerodynamic Forces and Structural Analysis

At the first time step, the initial condition defines the plate's position as it undergoes a step change at time = 0 s, and a steady case of aerodynamic loading is solved assuming the plate is rigid and fixed at the position specified by the initial condition. The simulation continues until the pressure distribution along the plate reaches convergence.

Then, the simulation starts time marching where at each time step, the aerodynamic solver computes the aerodynamic forcing along the plate from the deflection of the plate, then the structural solver computes the plate's response from the aerodynamic forcing and the plate's structural forcing using the ODE45 solver.

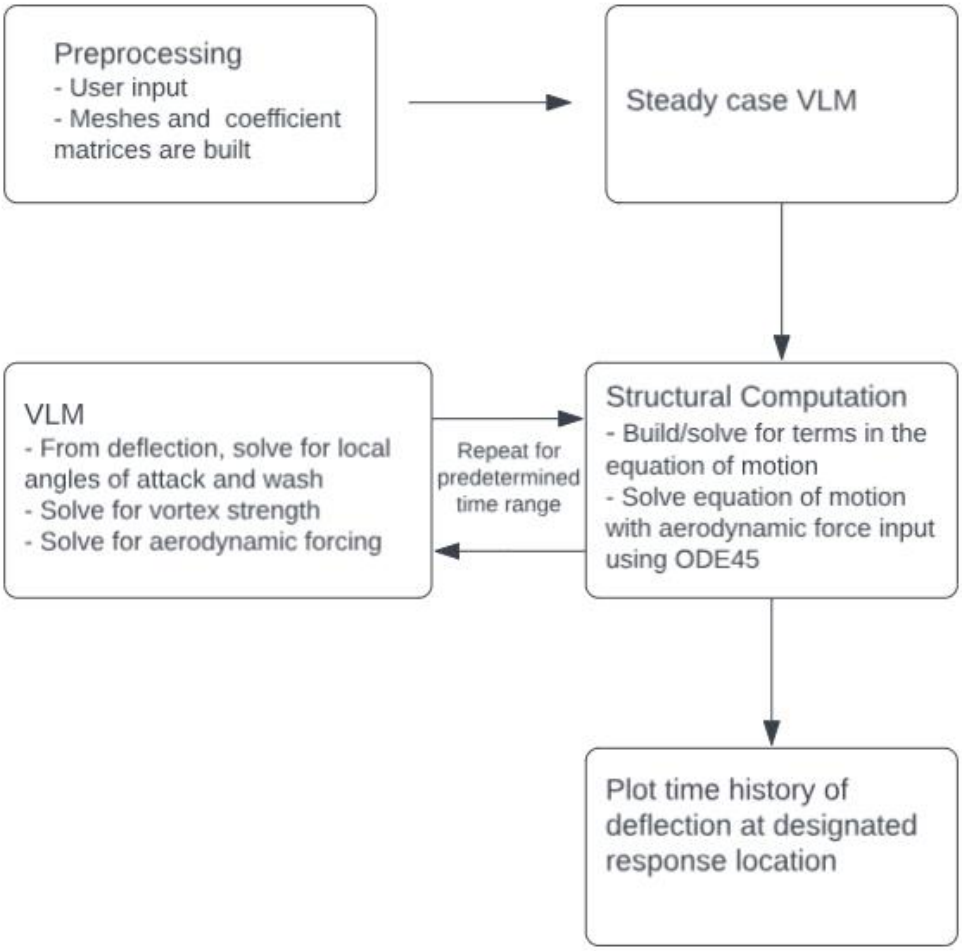

Figure 7: Flow chart describing the computational process for the coupled aeroelastic model

5. Computational Results for the Aeroelastic Model

5.1 Outputs

The completed model is tested with the same parameters as those from Table 1 except that the flow velocity has been altered. This is done to compare with experimental results obtained by Tang, Dowell, and Gibbs [9, 10], which also correspond to these parameters.

The initial condition of the plate is given as a step change at t = 0 s in the first mode only and starts with a nondimensional tip deflection of 0.25. Two modes were used in all three coordinates to produce the following results for time efficiency, which will only deliver a qualitative description of the aeroelastic behavior of the cantilevered plate. Regardless, it provides a rough estimate of the critical speed for flutter and the velocity range for LCO. Figures 8 and 9 show the time history of plate tip deflection, taken at the symmetry plane, at U = 24 m/s and 25 m/s, respectively.

It is seen that for U = 24 m/s, the plate's physical response is small and damps out given enough time, whereas at U = 25 m/s, the aeroelastic system is clearly beyond the critical flutter speed as the system enters LCO with a high amplitude of ~0.85.

Results for a range of velocities, mainly between 24 m/s and 25 m/s, are then produced and examined. The data presented in Figure 10 suggests that flutter started to occur at around 24 m/s. Wind tunnel experiment results from Tang and Dowell's work [9] indicate the flutter speed for this plate to be 21.35 m/s, suggesting that the computational solution is fairly close considering only 2 modes are used.

Furthermore, the LCO frequency at these varying velocities are also noted in Figure 11; all the data points lie between the 1st mode and 2nd mode bending natural frequencies. The computational solution shows the LCO frequency to be about 15.1 Hz, whereas experimental and theoretical results from Gibbs et al [10] suggests this value to be about 20 Hz.

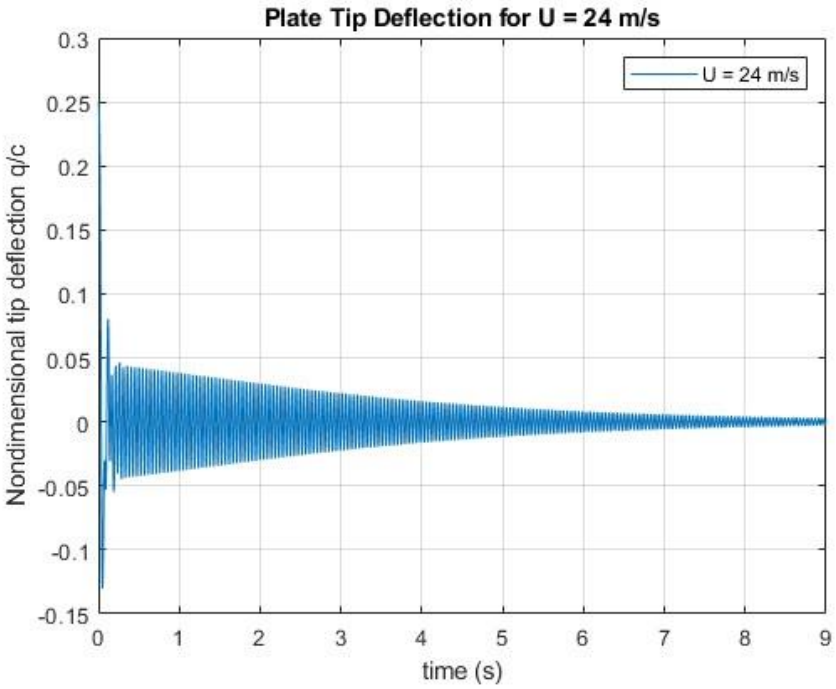

Figure 8: Time history of plate tip deflection at U = 24 m/s

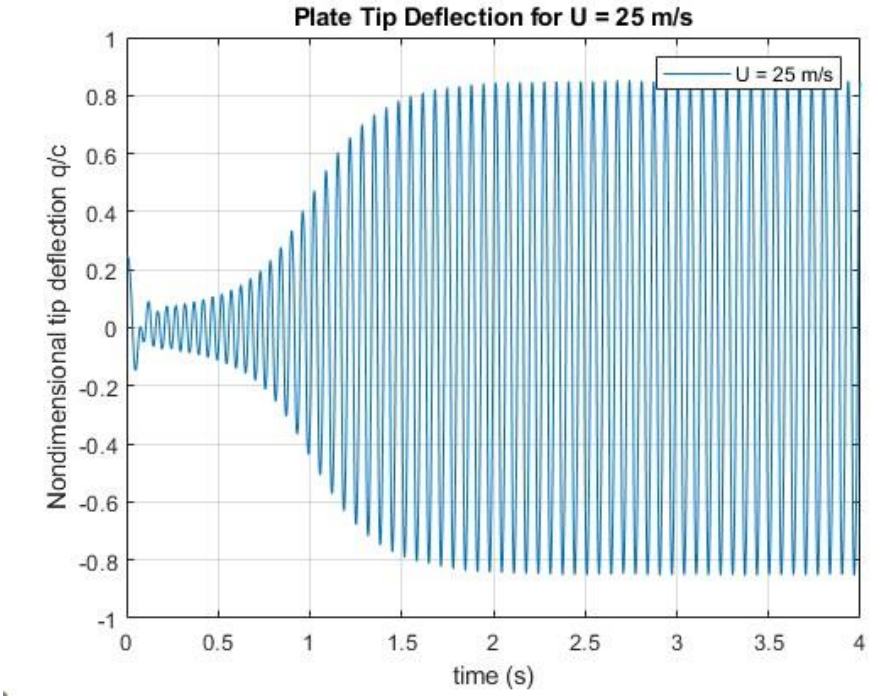

Figure 9: Time history of plate tip deflection at U = 25 m/s

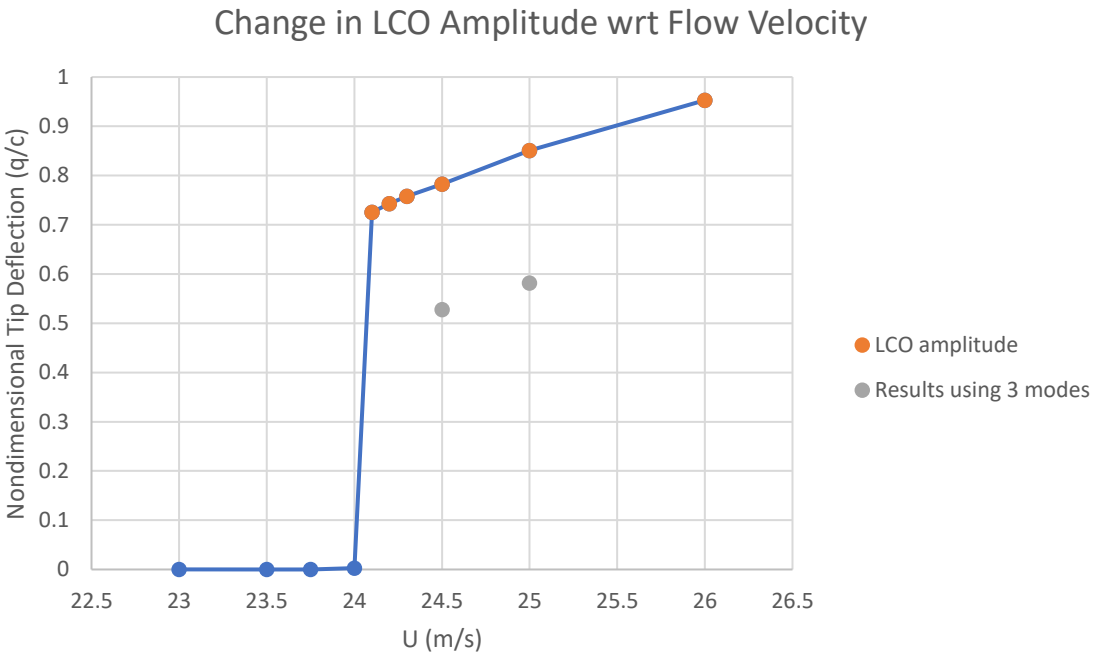

Figure 10: Plotting the change in LCO amplitude with respect to the flow velocity at 2 modes in the transverse direction

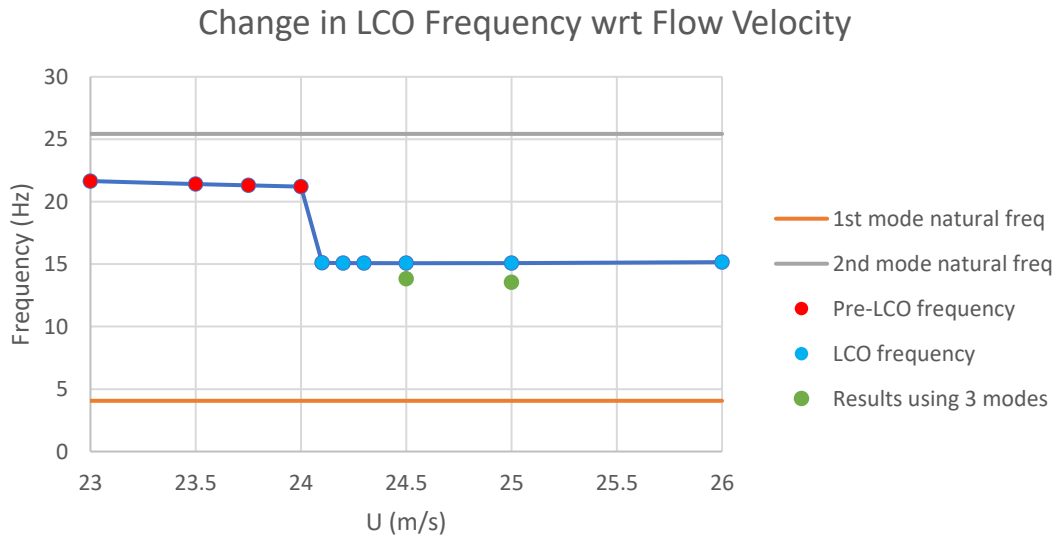

Figure 11: Plotting the change in LCO frequency with respect to the flow velocity at 2 modes and compared with the bending natural frequencies

Table 2: Flutter speed and frequency results

	Computational Model (2 modes)	Experimental
Flutter speed (m/s)	24	21.35
Flutter frequency (Hz)	15.1	20

Table 3: Natural bending frequencies of the plate

	ω (Hz)
1st Mode	4.06
2nd Mode	25.43
3rd Mode	71.20
4th Mode	139.53
5th Mode	230.65

5.2 Uncertainties and Limitations

At first sight, the computational results are decently close to the experimental flutter speed found in Tang and Dowell's study, but when examining the LCO amplitude curve generated from this thesis and [9], the amplitudes found in this paper are much greater than ones from the experiment, a discrepancy possibly caused by the low number of modes used in the present study. The computational LCO frequency also shows a difference of about 25% compared with results from [10]. As mentioned, using only 2 modes for the computational model can reduce the accuracy of the results, but it provides qualitative results. In addition, the results were generated with only 20 vortex elements along the chord of the plate, another limitation that adds uncertainty to the accuracy of the solution.

Increasing the number of modes and the number of vortices along the plate enhances the accuracy of the computation, but this option will be more costly. The choice between computation accuracy and speed is a problem which future work needs to address.

Meanwhile, computing with increasing number of modes and vortices with this model is in progress with the goal to find the least number of either for which the results will converge.

6. Conclusions

This thesis proposed an aeroelastic model created for a cantilevered plate system by combining an aerodynamic model, implemented using VLM, and a structural model, derived from the Lagrange method and the Rayleigh-Ritz method. The resulting computational model is capable of predicting the physical response along the plate.

Results produced by this model were shown for a low mode number case at varying flow velocities; the data collected reveals trend between LCO amplitude and velocity, and between LCO frequencies and velocity, allowing one to observe the transition to flutter and LCO. Calculations produced by this model provide reasonable results when compared with results from past studies, though their accuracy is still uncertain due to lack of data from using higher number of modes and a larger number of vortices along the chord of the plate. Regardless, the computational results provided a good qualitative description of the physical model at a relatively low computation cost.

As a natural next step, computations with higher numbers of modes and vortices will be tested. In addition, as mentioned in the introduction, this computational model was motivated by research on energy harvesting from structures vibration in LCO using piezoelectric components. The next goal for this tool is to predict the energy output when this model is equipped with piezoelectric patches, then reversing the inputs: calculating the optimal plate geometry which would maximize the energy output. Currently, the incorporation of piezoelectric components in the computation model is in progress, and wind tunnel tests for validation of computation results are on schedule. Other related works [11, 12] may also benefit from the development in the present study.

References

[1] Tang, D. M., Dowell, E. H., “Aeroelastic response and energy harvesting from a cantilevered piezoelectric laminated plate”, Journal of Fluids and Structures, Volume 76, 2018, pp. 14-36

[2] Dunnmon, J. A., et al, “Power extraction from aeroelastic limit cycle oscillations”, Journal of Fluids and Structures, Volume 27, Issue 8, 2011, pp. 1182-1198

[3] Hall, Kenneth C. “Eigenanalysis of unsteady flows about airfoils, Cascades, and Wings”. AIAA Journal. Vol. 32, No.12, 1994, pp. 2426-2432

[4] Huang, Wei, et al. (2016). “Dynamic Course Stability of Towing Systems Using Fiber Ropes”, MOSS, pp. 333-344, Sep. 2016.

[5] Tang, Deman M., et al. “Flutter and limit cycle oscillations of two-dimensional panels in three-dimensional axial flow”. Journal of Fluid and Structures. Vol. 17, No.2, 2003, pp. 225-242

[6] Tang, D., et al, “Inextensible Beam and Plate Theory: Computational Analysis and Comparison With Experiment,” *ASME J. Appl. Mech.*, 81(6), 2014, p. 061009

[7] Dowell, E. H., McHugh, K., “Equations of Motion for an Inextensible Beam Undergoing Large Deflections,” ASME J. Appl. Mech., 83(5), 2016, p. 051007

[8] McHugh, K., Dowell, E. H., "Nonlinear Responses of Inextensible Cantilever and Free–Free Beams Undergoing Large Deflections." ASME. *J. Appl. Mech*., 85(5): 051008, 2018

[9] Tang, D.M., Dowell, E. H. “Experimental Aeroelastic Models Design and Wind Tunnel Testing for Correlation with New Theory”. *Aerospace*. 3(2):12. 2016

[10] Gibbs, S. Chad, et al, “Aeroelastic stability of a cantilevered plate in yawed subsonic flow, Journal of Fluids and Structures”, Volume 49, 2014, pp. 450-462

[11] Wang, Ivan. “Aeroelastic and Flight Dynamics Analysis of Folding Wing Systems”. Dissertation, Duke University. 2013.

[12] Freydin, M., et al, “Response of a plate with piezoelectric elements to turbulent pressure fluctuation in supersonic flow”, Journal of Fluids and Structures, Volume 114, 2022, 103696.